Journal of Materials Chemistry A

ROYAL SOCIETY OF CHEMISTRY

PAPER

View Article Online
View Journal | View Issue

Cite this: J. Mater. Chem. A, 2021, 9, 10354

Size-dependent hydrogen trapping in palladium nanoparticles†

Wang Liu,[a] Yann Magnin,[bc] Daniel Förster,[de] Julie Bourgon,[a] Thomas Len,[f] Franck Morfin,[f] Laurent Piccolo,[f] Hakim Amara *[dg] and Claudia Zlotea *[a]

We report an experimental study, supported by a theoretical approach based on simulations, to explore the phenomenon of H trapping in small Pd nanoparticles. Hydrogen absorption/desorption of a series of Pd nanoparticles with different average sizes (6.0, 2.0 and 1.4 nm) is only partially reversible, as proven by pressure-composition-isotherms at 25 °C. The irreversible H amount is trapped into strong interstitial sites. *In situ* EXAFS was employed to highlight the local structural changes and the H trapping inside the volume of Pd nanoparticles. We evidence a double size-dependent effect of H trapping inside Pd nanoparticles: the smaller the Pd particle size, the larger the amount of trapped H and the higher the binding energy experienced by H atoms. For example, 26% of the initial H capacity is trapped in Pd nanoparticles with 2.0 and 1.4 nm average sizes and a treatment under vacuum above 150 °C is needed to fully desorb the trapped H. To get atomic-scale insights into the location of the trapping sites, we perform both density functional theory and tight-binding calculations. These simulations show that the strong H trapping sites are the octahedral interstitials located at the subsurface of Pd nanoparticles where high relaxations are possible. This finding might clarify the controversial role of "subsurface or bulk" hydrogen in Pd-based nano-catalysts in several hydrogenation reactions.

Received 15th December 2020
Accepted 6th April 2021

DOI: 10.1039/d0ta12174f

rsc.li/materials-a

Introduction

Many physicochemical parameters of transition metals have been reported to be size dependent based on both experiments and theoretical modelling. It has been shown that the size reduction, consisting in increasing the specific surface of particles – as compared to their volume – has a great impact on their performances for a wide range of energy applications, as hydrogen storage, hydrocarbon reforming *etc.*[1] The particle size reduction shows important changes in the lattice parameters, the binding energy, the bulk modulus, and the melting point, when compared to the bulk phase. Moreover, these changes have proven to scale linearly with the inverse of the size of the nanostructure.[2]

The case of Pd nanoparticles is emblematic since it possesses a simple lattice (face centered cubic – fcc), also adopted by other noble metals. Alongside with modifications of physicochemical properties such as, the fcc lattice parameter,[3–5] significant changes of hydrogen absorption in Pd with decreasing the particle size have been reported. Furthermore, it is well known that Pd is the only noble metal that absorbs hydrogen and forms a hydride (β phase) below 1 bar at room temperature.[6] At low H_2 pressure, below the one needed for hydride formation, a dilute solid solution of hydrogen within Pd is formed, corresponding to the α phase. These two phases are separated by a miscibility gap, where they coexist. Following the Gibbs phase rule, the equilibrium pressure is constant at fixed temperature during the hydride phase formation (a plateau pressure is noticed in the pressure-composition-isotherms, PCI). Important modifications of the hydrogen sorption properties with decreasing the Pd particle size have been reported: improved kinetics, modified thermodynamics and changes in the Pd–H phase diagram.[7–10] The overwhelming experimental studies and numerous reviews[8,11–13] agree to describe the following features: the hydrogen solubility in the solid solution (α phase) enhances by decreasing the size while the hydrogen solubility in the hydride phase (β phase) diminishes with reducing the particle size. Consequently, the miscibility gap (α to β region) narrows and the critical temperature, T_C (defined as

[a]Université Paris Est, Institut de Chimie et des Matériaux Paris-Est (UMR7182), CNRS, UPEC, 2-8 Rue Henri Dunant, 94320 Thiais, France. E-mail: claudia.zlotea@icmpe.cnrs.fr

[b]MIT, Energy Initiative, Massachusetts Institute of Technology, Cambridge, MA, USA

[c]Consultant, Total@Saclay NanoInnov, 2 Boulevard Thomas Gobert, 91120 Palaiseau Cedex, France

[d]Laboratoire d'Etude des Microstructures, ONERA-CNRS, UMR 104, Université Paris Saclay, BP 72, Chatillon Cedex, 92322, France. E-mail: hakim.amara@onera.fr

[e]CINaM-UMR 7325, CNRS-Aix Marseille Université, Campus de Luminy-Case 913, 13288, Marseille Cedex 09, France

[f]Univ Lyon, Université Claude Bernard – Lyon 1, CNRS, IRCELYON – UMR 5256, 2 Avenue Albert Einstein, 69626 Villeurbanne CEDEX, France

[g]Laboratoire Matériaux et Phénomènes Quantiques, Université de Paris-CNRS, Case Courrier 7021, F-75205, Paris Cedex 13, France

† Electronic supplementary information (ESI) available. See DOI: 10.1039/d0ta12174f

the temperature where the hysteresis between the absorption and desorption curves vanishes) in the phase diagram decreases.[14] Overall, all studies converge to a decrease of the total hydrogen sorption capacity in the hydride phase with reducing the Pd particle size. To understand this behaviour several possible explanations have been proposed. The most widespread hypothesis emphasizes a core/shell model with a subsurface shell in which interstitial sites are less favourable for hydrogen atoms and a bulk-like inner core that more easily absorb hydrogen to form a bulk-like hydride. Thus, the number of interstitial sites available for hydrogen and the volume that will transform into the hydride phase reduce with decreasing the size.[8,15,16] Other explanations make use of size-induced thermodynamic modifications (entropy and enthalpy of mixing)[17] or stress-induced changes (surface tension for nanoparticles or clamping effect for thin films).[18,19] In a very simple view, the miscibility gap shifts to lower temperatures and consequently, the solubility limit on the α phase increases, whereas the one in the β phase decreases. Thus, the total sorption capacity of Pd nanoparticles drops as compared to the bulk.

Theoretical approaches of the size-dependence of the hydrogen absorption properties in Pd are scarce and generally based on the core/shell model.[20–22] An empirical force-field model, such as ReaxFF, has been employed for modelling hydride formation in 1.0, 1.5 and 2.0 nm-sized Pd revealing that reducing the cluster size leads to a narrowing of the miscibility gap,[20] in agreement with experiments. Other theoretical studies have also shown an enhanced hydrogen solubility in the solid solution with hydrogen segregation to the subsurface and a vanishing of phase transition for 2 nm Pd clusters.[21]

It is noteworthy that changes of hydrogen sorption properties in nanosized Pd are well-known and largely documented from both experimental and theoretical approaches. While hydrogen absorption is widely explored, desorption has been less studied. The latter is mentioned in the context of pressure-composition-isotherms showing a hysteresis between absorption and desorption branches. Previously it was observed that absorption and desorption show only partial reversibility, *i.e.* non-closing absorption/desorption PCI curves, for Pd nanoparticles.[23–25] Interestingly, highly deformed bulk Pd[26] undergoes similar phenomenon. This behaviour is ascribed to the hydrogen trapping in strong sites of the lattice. Defects (mainly dislocations and vacancies) are the main H trapping sites in bulk metals and the interaction between H and defects is of paramount importance in the embrittlement process of materials.[27] If defects can be easily encountered in bulk materials, they are less favourable in small nanoparticles. Therefore, the classical explanation of H trapping in defects is unlikely for nanoparticles.

The topic of H trapping was earlier addressed for Pd nanoparticles with average sizes of 2.5 nm,[28] 3.6 nm (ref. 29) and 6.1 nm.[30] Mainly experimental observations were reported and only few tentative explanations were proposed. Using a Gibbs approach for the construction of the absorption isotherm for 3.6 nm Pd nanoparticles, Ren and Zhang suggested that the responsible sites for H trapping are located within a surface shell of around 0.4 nm.[29] Moreover, another study claims an irreversible trapping of H atoms inside 2.5 nm Pd nanoparticles, *i.e.* desorption is uncomplete even at temperatures as high as 140 °C.[28]

Recently, Wagner and Pundt proposed a model for the determination of the distribution of site energies in Pd–H thin films in the solid solution regime.[31] Interstitial sites, grain/domain boundary sites and deep traps could be distinguished. If dislocations and vacancies have a minor contribution to H trapping in thin films, the authors claimed that deep traps are related to the surface adsorption sites.

In this context, the surface seems to play an important role for H trapping in nanostructured materials. However, the surface mechanisms driving these effects are still unclear, especially at the atomic scale. Indeed, several open questions arise in the case of nanoparticles: which strong sites are responsible for trapping H in nanoparticles? Is H trapping size dependent? Can trapped H be desorbed from nanoparticles?

Here, we report on the hydrogen absorption/desorption into a series of Pd nanoparticles supported on porous carbon with average sizes of 1.4, 2.0 and 6.0 nm. Our study is based on both experimental and theoretical approaches with a focus on H trapping and its size-dependency in nanoparticles. A thorough investigation by *in situ* X-ray Absorption Spectroscopy (XAS) provides a fine and unique local probe of the structural change during isothermal H absorption and desorption at 25 °C. In order to avoid any artefacts (oxide formation, impurities) during EXAFS refinements, a robust and clean pre-treatment procedure was established. The experimental results are supported at the atomic level by using both Tight-Binding Monte Carlo simulations (TB-MC) and Density Functional Theory calculations (DFT) showing the key role played by subsurface sites in the desorption mechanism.

Materials and methods

Well dispersed Pd nanoparticles with an average size of 6.0, 2.0 and 1.4 nm supported on a porous graphite (High Surface Area Graphite – HSAG – with 500 $m^2\ g^{-1}$ from Imerys Graphite & Carbon) and a commercial activated carbon (AC with 1400 $m^2\ g^{-1}$ from STREM Chemicals) were prepared by a wet impregnation method followed by H_2 reduction at either 500 or 300 °C, as reported earlier.[32] The 6.0 and 2.0 nm Pd nanoparticles were supported on graphite, whereas the 1.4 nm clusters were synthesized on activated carbon. The final metal amount was 10 wt% over the whole composite weight. Transmission Electron Microscopy (TEM) characterisations were carried out with a 200 kV FEG microscope (FEI Tecnai F20 equipped with a Gatan Energy Imaging Filter, resolution 0.24 nm). The Pd nanoparticle size distribution and the average size were determined by statistical analyses of several TEM images.

The structural properties of Pd nanoparticles were determined by powder X-ray diffraction (XRD) using a D8 Advance Bruker diffractometer (Cu K_α radiation, Bragg–Brentano geometry). *In situ* XRD was performed under 1 bar H_2 atmosphere and vacuum at ambient temperature.

To check the local structure of the Pd, *in situ* X-ray absorption spectroscopy (XAS) experiments were performed on the ROCK beam line at the SOLEIL synchrotron. The X-ray absorption spectra at the K edge of Pd were measured at isothermal conditions at 25 °C. The powder samples were placed inside a Lytle-type cell which was connected to a gas distribution system that controls the gas flow composition at atmospheric pressure.[33] Prior to any isothermal measurement the samples were treated under H_2 flow (30 ml min^{-1}) at room temperature for 10–15 minutes to remove any oxide at the surface of nanoparticles, as demonstrated earlier.[12] Then the H_2 flow was replaced by He (30 ml min^{-1}) and the samples were heat-treated with the following temperature profile: heating to 250 °C with a ramp of 10 °C min^{-1}, dwell at 250 °C for 10 minutes followed by cooling to 25 °C with a ramp of 15 °C min^{-1}. The purpose of this treatment is to completely remove water molecules formed during reduction of the surface oxide layer at room temperature together with hydrogen atoms possibly adsorbed/absorbed in Pd nanoparticles. Such pre-treatment ensures the exploration of hydrogen sorption properties of clean nanoparticles without oxide layer or other interstitial impurities. Four samples (bulk Pd and 6.0, 2.0 and 1.4 nm Pd nanoparticles) were measured under several H_2 partial pressures in a He flow (30 ml min^{-1}). The sequence of H_2 partial pressures was the following: 0, 0.05, 0.25, 0.5 and 1 bar in absorption as well as 1, 0.5, 0.25, 0.05 and 0 bar H_2 in desorption at 25 °C. A Pd foil was used as reference. All XANES spectra were calibrated in energy and normalised. The XAS data treatment and EXAFS refinements were performed with the MAX program package (E_0 = 24 350 eV for Pd K edge, Fourier transform range 3–15 $Å^{-1}$).[34,35] EXAFS fitting was performed on first-sphere filtered spectra. Theoretical phases and amplitudes were computed with FEFF8 based on fcc Pd metal structure. The refined parameters are the coordination number (N), the Debye–Waller factor (σ^2), the nearest neighbour distance (R_{Pd-Pd}) and, for small Pd nanoparticles only, the C_3 cumulant factor to account for deviations from Gaussian distribution. The energy shift ΔE_0 was refined first for the Pd reference and then fixed for further refinements. The goodness of fit was evaluated using the quality factor (QF).

Hydrogen absorption properties were determined by measuring the pressure-composition isotherms (PCI) at 25 °C up to 1 bar. The PCI curves were recorded using an automated volumetric device (Autosorb IQ Quantachrome). Before any sorption measurements, the samples were pre-treated with H_2 at 25 °C and then degassed under secondary vacuum at 220 °C overnight. The adsorption on the porous host is small under these conditions, as demonstrated previously.[36] Consequently, the sorption capacity is expressed here as H/Pd. Good repeatability of the measurement was observed.

The hydrogen desorption properties were investigated by thermo-desorption-spectroscopy (TDS) using a homemade instrument coupled to a quadruple mass spectrometer (MKS MicroVision Plus RGA) working under high vacuum, as described elsewhere.[37] The samples were pre-treated with H_2 at 25 °C and then degassed under secondary vacuum at 220 °C overnight. The samples were exposed to 1 bar H_2 pressure at room temperature, then evacuated and the desorbed H_2 partial pressure was recorded by heating constantly up to 225 °C with a constant heating ramp of 5 °C min^{-1}.

To go beyond phenomenological approaches, simulations at atomic scale were performed using both tight-binding (TB) and Density Functional Theory (DFT) calculations. In order to better understand the variation of the lattice parameter with the size of the NPs, we have chosen to perform TB calculations for several NP sizes (ranging from 55 to 2057 atoms) and shapes (cuboctahedra, icosahedra and truncated octahedra) in order to generalize our conclusions. The TB formalism framework is perfectly adapted to carry out this kind of complete study, which requires different types of nanoparticles made up of several hundreds of atoms. To describe transition-metal systems, we previously developed a model based on the TB approximation; details can be found elsewhere.[38] We use a moment (or recursion) method to determine the local electronic densities of states at a minimal (fourth moment) level, giving access to the band energy and ensuring linear scaling of the CPU time with system size. Such model is particularly well suited to model transition metals where the cohesion is governed by the d-electron band.[39] This interatomic potential is both fast and accurate once a set of parameters has been fitted to reproduce metal–metal interactions. The adjustment of the parameters is based on a fitting procedure already implemented in a previous study for empirical potentials[40] and generalized to the TB formalism at the fourth moment approximation used in this work. For the Pd system, the TB parameters were obtained by fitting on experimental values of the lattice parameter, the cohesive energy, and the elastic moduli (bulk modulus and the two shear moduli) for the fcc structure, as detailed in Table I of the ESI.† This TB model was implemented in a Monte Carlo (MC) code in the canonical ensemble, based on the Metropolis algorithm, which allows to relax the structures at finite temperatures.[41] In the canonical ensemble, MC trials correspond to random displacements. The average quantities were calculated over 10^6 MC macrosteps, a similar number of macrosteps being used to reach equilibrium. A MC macrostep corresponds to N propositions of random atomic displacement, N being the total number of atoms of the cluster. In addition, the location of the H trapped in the Pd nanoparticles and bulk fcc Pd was studied by DFT calculations which are very precise. We used the Quantum Espresso[42] code within the projector-augmented wave (PAW) method.[43] The generalized gradient approximation[44] was employed for all calculations. Two different particles containing 147 and 309 atoms in cuboctaedron shape were considered as well as bulk fcc structure. This equilibrium structure was chosen because it is typical of the shapes observed experimentally. In the case of NPs, the size of the supercell in the all directions was set to 40 Å to avoid artefacts due to interaction between images caused by periodic boundary conditions. For the bulk fcc, integrations over the Brillouin zone were based on a 6 × 6 × 6 Monkhorst–Pack three-dimensional grid for 108 atom cells. Calculations were performed at zero pressure, *i.e.*, the relaxation of the atoms and the shape of the simulation cell were considered using the conjugate gradient minimization scheme. In all cases (NPs and bulk fcc), the atomic positions were relaxed until the magnitude

of the forces on all the atoms was smaller than 1×10^5 Ha Bohr^{-1}.

Results

Pd nanoparticles are well dispersed on the carbon supports, as shown in Fig. 1. The average particle sizes are 6.0 nm ($\sigma = 1.5$ nm) for HSAG support and $T_{red} = 500$ °C, 2.0 nm ($\sigma = 0.5$ nm) for HSAG support and $T_{red} = 300$ °C and 1.4 nm ($\sigma = 0.3$ nm) for AC support and $T_{red} = 300$ °C, where σ is the standard deviation of the statistical analysis. More TEM images are shown in Fig. SI-1.†

Pressure-composition-isotherms (PCI) during hydrogen sorption at 25 °C are displayed in Fig. 2.

The size effect on PCI can be summarised as follows: the total capacity at 1 bar H_2 pressure diminishes, the miscibility gap narrows, the plateau is slopping until complete vanishing for the smallest size (1.4 nm) and the solubility in the α phase increases with decreasing the particle size. The presence of a plateau in the PCI, even slopped, marks the formation of a hydride phase for bulk, 6.0 and 2.0 nm particles. The vanishing of the plateau for 1.4 nm clusters confirms that the hydride phase is no longer formed and only solid solutions with H are expected, in very good agreement with our previous findings for 1.0 nm Pd clusters embedded into MIL-101.[14] Along with these observations, we also notice that all Pd nanoparticles show incomplete recovery between the absorption and desorption branches at low pressures, contrary to bulk Pd. The non-closing absorption/desorption PCI branches are often encountered for Pd nanoparticles and H trapping inside the lattice is suggested to explain this finding.

In order to better understand this behaviour, we have performed *in situ* XRD under vacuum (initial state), under 1 bar H_2 (absorbed state) and again under vacuum (desorbed state) at 25 °C (Fig. SI-2†). All diffraction peaks could be indexed into a fcc structure typical for bulk metal. As expected, the diffraction peaks became broader with reducing the particles size. With one exception for 1.4 nm nanoparticles, a reversible peak shift is noticed during absorption and desorption steps.

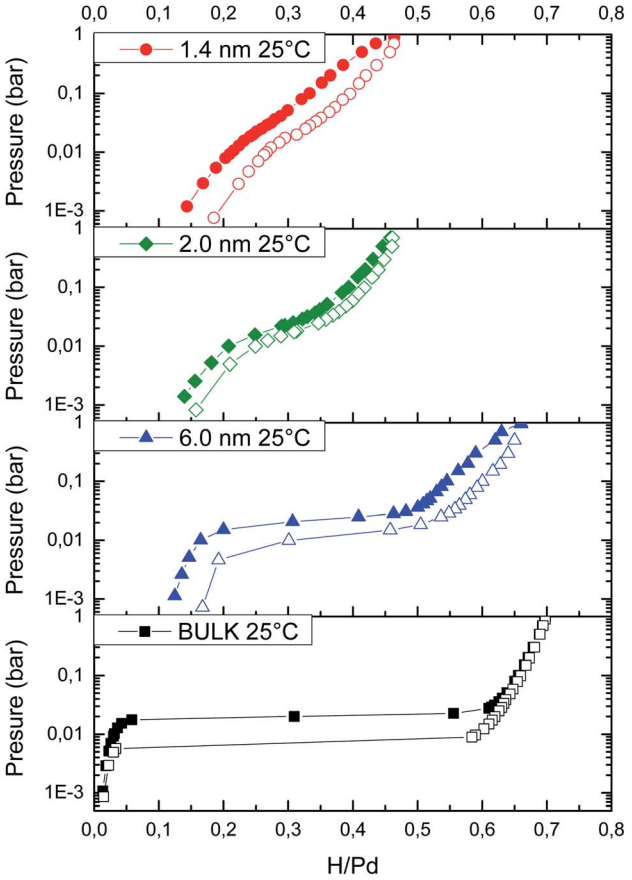

Fig. 2 Pressure-composition-isotherms for bulk Pd (square) and Pd nanoparticles with average sizes of 6.0 nm (triangle), 2.0 nm (rhombus) and 1.4 nm (circle) at 25 °C. Full and empty symbols stand for absorption and desorption, respectively.

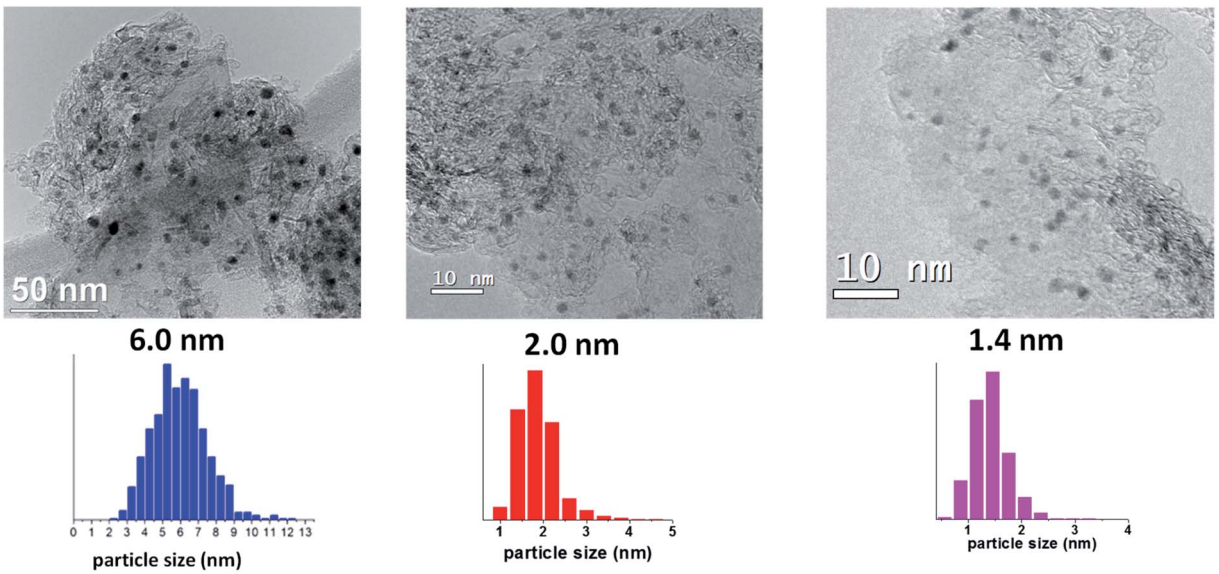

Fig. 1 TEM images and related particle size histograms for 6.0 nm, 2.0 nm and 1.4 nm Pd nanoparticles supported on carbon.

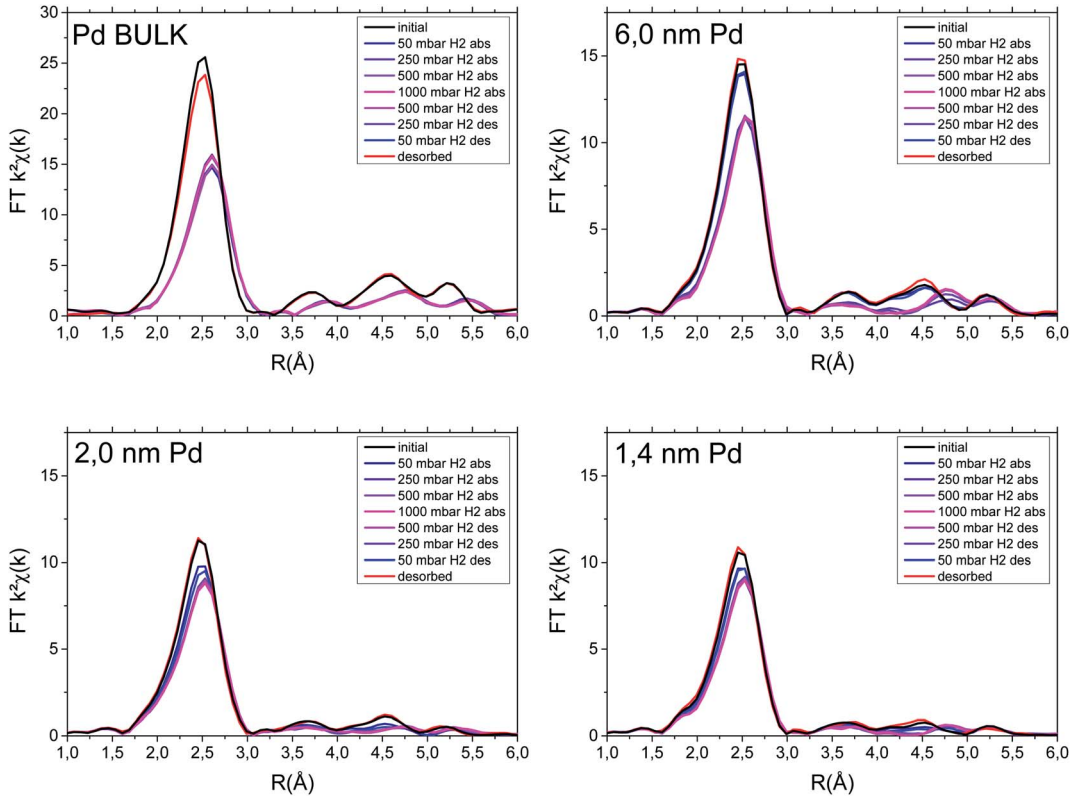

Fig. 3 FT of the EXAFS spectra ($k^2\chi(k)$) for bulk Pd and 6.0, 2.0 and 1.4 nm Pd nanoparticles under various partial pressures of H_2 at 25 °C.

From this experiment, nothing can be inferred about the possible trapping of H inside the lattice of nanoparticles after desorption due to large peaks and uncertainties in the XRD analysis. Thus, a finer probe must be employed to characterize the H trapping inside Pd nanoparticles.

Consequently, we have performed *in situ* EXAFS measurements on clean Pd nanoparticles, *i.e.* without oxide layer at the surface and other impurities inside the volume of nanoparticles. The special pre-treatment detailed in the Materials and methods section ensures clean Pd nanoparticles, *i.e.* surface and volume free of any impurity, which is essential to emphasize possible subtle evolution of nearest Pd–Pd neighbouring distances as function of H absorption and desorption. These experiments have been carried out under several H_2 partial pressures: 0, 50, 250, 500 and 1000 mbar in absorption as well as, 500, 250, 50 and 0 mbar in desorption under isothermal conditions at 25 °C. Fig. 3 shows the Fourier Transform (FT) of EXAFS spectra for bulk Pd, 6.0, 2.0 and 1.4 nm Pd nanoparticles under different H_2 partial pressures at 25 °C. Overall, FT peaks shift to larger distances and their intensity decreases with increasing H pressure, irrespective of particle size. The latter observation is size dependent: the smaller the size, the minor the effect on FT.

The EXAFS refinements allow the determination of the nearest Pd–Pd distance (R_{Pd-Pd}), the coordination number (N) and the Debye–Waller factor (σ^2), see Table 1. Typical refinements are plotted in Fig. SI-3.†

The average coordination number (average of all experimental points) decreases from 11.5 for bulk (12 typical for bulk fcc metals) to 10.3, 7.9 and 7.5 for 6.0, 2.0 and 1.4 nm Pd nanoparticles, respectively. The decrease of N can be understood by an enlarged number of dangling bonds of surface atoms increasingly important with decreasing the size.[12,14] The initial value of the Debye–Waller factor shows an increase from 0.0066 to 0.0087 from bulk to 1.4 nm particle size. This finding can be explained as an increase of the static disorder in nanoparticles due to the relaxation of bond lengths at the surface, which undergoes substantial strain. Moreover, within the same material, the Debye–Waller factor rises with increasing the hydrogen pressure, which can be linked to the hydride phase formation and consequently, to the rise of the static disorder by hydrogen insertion within the interstitials. It is worth noticing that the coordination numbers and Debye–Waller factors do not differ significantly for 2.0 and 1.4 nm nanoparticles because the discrimination among these sizes is within the error bar by this experimental technique.

It is interesting to notice that the initial R_{Pd-Pd} (clean surfaces and H-free nanoparticles after heat-treatment, as described above) for 6.0 and 2.0 nm particles are similar to the bulk value (2.748(1) Å). For 1.4 nm clusters, the initial R_{Pd-Pd} is slightly smaller than the bulk value (2.745(1) Å).

Comparisons between the PCI curves and the R_{Pd-Pd} as function of pressure are shown in Fig. SI-4.† A good agreement is noticed between the PCI curves and the evolution of R_{Pd-Pd} as function of pressure, irrespective of the particle size.

A thorough analysis of the refinements results in Table 1 allows us to draw several remarks:

(1) For bulk Pd the absorption/desorption is fully reversible.

Table 1 EXAFS refinements results for bulk Pd and 6.0, 2.0 and 1.4 nm Pd nanoparticles under various H_2 pressures at 25 °C. The nearest Pd–Pd distance (R_{Pd-Pd}), the coordination number (N), the Debye–Waller factor (σ^2), C_3 cumulant and the confidence factor (QF) are given

Sample	H_2 pressure (mbar)	R_{Pd-Pd} (Å)	N	σ^2 (Å^2)	C_3 (10^{-4} Å^3)	QF
Bulk	0	2.748(1)	11.5(5)	0.0066(1)	—	1.4
	50	2.842(1)	11.5(5)	0.0088(1)	—	0.8
	250	2.848(1)	11.5(5)	0.0084(1)	—	1.5
	500	2.849(1)	11.5(5)	0.0084(1)	—	1.5
	1000	2.852(1)	11.5(5)	0.0084(1)	—	1.4
	500	2.850(1)	11.5(5)	0.0087(1)	—	1.3
	250	2.848(1)	11.5(5)	0.0087(1)	—	1.3
	50	2.842(1)	11.5(5)	0.0087(1)	—	1.2
	0	2.747(1)	12.0(5)	0.0072(1)	—	2.3
6.0 nm	0	2.748(1)	10.4(5)	0.0076(1)	—	3.3
	50	2.804(1)	10.2(5)	0.0090(2)	—	2.1
	250	2.823(1)	10.2(5)	0.0086(2)	—	2.3
	500	2.826(1)	10.2(5)	0.0086(2)	—	2.3
	1000	2.828(1)	10.2(5)	0.0086(2)	—	2.3
	500	2.826(1)	10.3(5)	0.0086(2)	—	2.4
	250	2.824(1)	10.2(5)	0.0086(2)	—	2.3
	50	2.816(1)	10.2(5)	0.0086(2)	—	2.2
	0	2.758(1)	10.4(5)	0.0076(2)	—	3.2
2.0 nm	0	2.748(1)	7.6(5)	0.0085(2)	1.1(4)	3.5
	50	2.777(1)	7.7(5)	0.0091(2)	1.1(4)	1.9
	250	2.793(1)	7.9(5)	0.0098(2)	1.1(4)	2.1
	500	2.797(1)	8.0(5)	0.0098(2)	1.1(4)	2.3
	1000	2.799(1)	8.0(5)	0.0098(2)	1.5(4)	2.5
	500	2.798(1)	8.0(5)	0.0097(2)	1.1(4)	2.1
	250	2.795(1)	8.1(5)	0.0097(2)	1.1(4)	2.4
	50	2.785(1)	7.9(5)	0.0094(2)	1.1(4)	2.1
	0	2.768(1)	7.8(5)	0.0086(2)	1.5(4)	2.2
1.4 nm	0	2.745(1)	7.5(5)	0.0087(2)	1.1(3)	1.9
	50	2.772(1)	7.5(5)	0.0090(2)	1.1(3)	1.5
	250	2.789(1)	7.5(5)	0.0095(3)	1.1(3)	1.2
	500	2.794(1)	7.6(5)	0.0094(3)	1.1(3)	1.1
	1000	2.798(1)	7.5(5)	0.0094(3)	1.1(3)	1.1
	500	2.795(1)	7.4(5)	0.0093(3)	1.1(3)	1.1
	250	2.792(1)	7.5(5)	0.0093(3)	1.1(3)	1.0
	50	2.779(1)	7.6(5)	0.0091(2)	1.1(3)	1.3
	0	2.764(1)	7.5(5)	0.0087(2)	1.1(3)	1.3

(2) For all Pd nanoparticles the values of R_{Pd-Pd} after desorption are all systematically larger than the initial ones: 2.758 *vs.* 2.748 Å for 6.0 nm particles, 2.768 *vs.* 2.748 Å for 2.0 nm particles and 2.764 *vs.* 2.745 Å for 1.4 nm particles.

These findings are in good agreement with PCI curves proving that hydrogen absorption/desorption is not fully reversible in nanoscaled Pd and H is irreversibly trapped inside the lattice of nanoparticles. Moreover, the larger R_{Pd-Pd} observed after desorption suggests that H is trapped inside the volume of nanoparticles and not at the surface as adsorbed species, as recently suggested for Pd thin films.[31] This is supported by the hypothesis that H atoms chemisorbed at the surface of Pd nanoparticles have a negligible effect on the overall nearest neighbour distances determined by EXAFS.

To highlight the size dependence of this behaviour Fig. 4 displays the evolution of R_{Pd-Pd} as function of the inverse of particle size in three states: initial clean metal, absorbed state under 1 bar of H_2 and desorbed state under He. Obviously, there

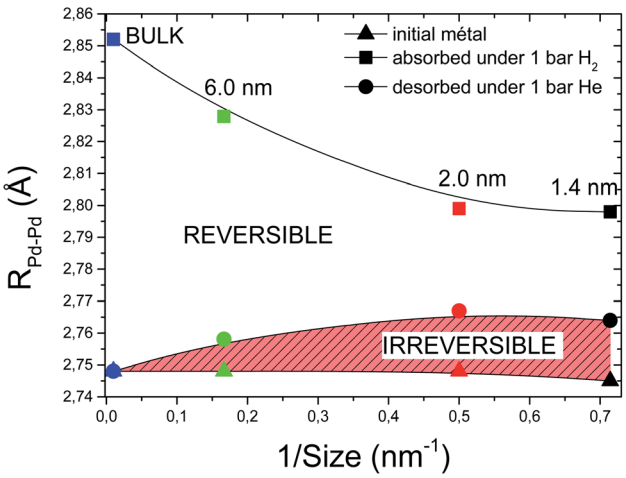

Fig. 4 The variation of R_{Pd-Pd} as function of the inverse of particle size for several sizes of bulk Pd and nanoparticles as initial metal (triangle), hydride (square) and desorbed phase (circle).

is a size dependence of the quantity of trapped H (irreversible part): the smaller the size, the larger the irreversible H amount (the dashed area in Fig. 4).

However, one might object that nanoparticles are possibly not fully desorbed because of kinetic issues rather than H trapping, although this may seem counterintuitive since kinetics of hydrogen desorption for nanoparticles are enhanced relative to bulk. We have demonstrated that our results listed in Table 1 were obtained at thermodynamic equilibrium (see Fig. SI-5† and related comments). No kinetic effects are responsible for the observed trend in the R_{Pd-Pd}.

In order to check if H trapped inside Pd nanoparticles can be desorbed at high temperature, we have performed *in situ* EXAFS under He flow during heating to 250 °C (10 °C min^{-1}) and TDS experiments under dynamic vacuum for all samples (5 °C min^{-1}). The results of EXAFS refinements (nearest neighbour distance) and the TDS spectra are plotted in Fig. 5a and b, respectively.

The nearest neighbour distance for bulk Pd steadily increases in agreement with the expected linear thermal expansion of metallic Pd (dotted line in Fig. 5a). Pd nanoparticles show a different behaviour with first a contraction of the nearest neighbour distance up to 150–170 °C, followed by a linear rise almost parallel to the linear thermal expansion of Pd metal. This finding is in line with the TDS results showing H desorption peaks for all Pd nanoparticles with the maximum desorption rate in between 75–110 °C, contrary to bulk Pd that does not show any desorption at high temperature. In summary, all our experimental results converge to conclude that H trapping occurs in 6.0, 2.0 and 1.4 nm Pd nanoparticles unlike bulk metal. Trapped H can be desorbed by heating to 150–170 °C under vacuum or inert gas flow.

A close inspection of the maximum desorption rates for Pd nanoparticles (maximum of desorption peaks in the TDS – Fig. 5b) suggests a clear size effect: the smaller the size, the higher the desorption temperature. This suggests that trapped

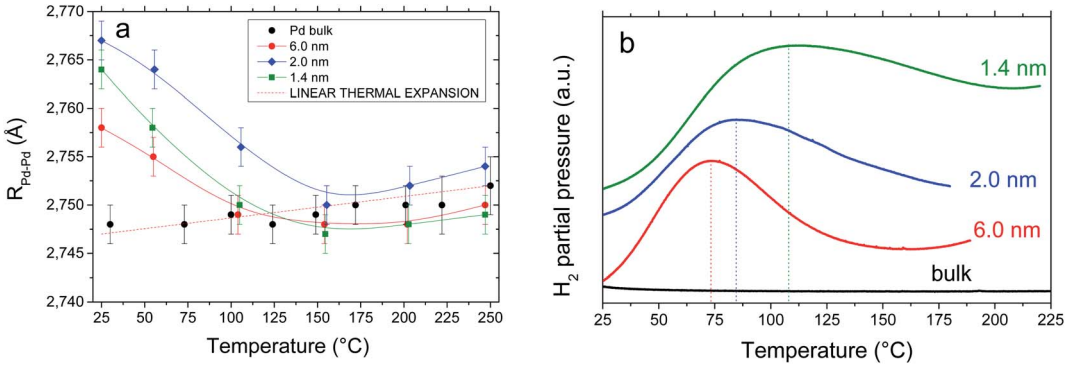

Fig. 5 The thermal variation of R_{Pd-Pd} (a) and the TDS spectra (b) for bulk, 6.0, 2.0 and 1.4 nm Pd nanoparticles. In (a), the expected linear thermal expansion of bulk Pd is also plotted.

H in smaller nanoparticles occupies stronger binding sites than in larger particles, *i.e.* a large activation energy is required for desorbing trapped H from small nanoparticles.

Discussion

Lattice parameters of nanoparticles

Experimentally, contradictory trends have been earlier claimed in the lattice parameter of Pd nanoparticles with particle size: both lattice contraction[3,5] and expansion[45] have been reported with decreasing the nanoparticle size, as compared to the bulk value. The decreasing trend can be understood by the increased number of under-coordinated atoms at the surface those bond lengths shrink spontaneous; consequently, the hydrostatic pressure induced by surface tension results in lattice contraction and strain, which is increasingly important with decreasing the size. The increase in lattice parameter was previously explained by pseudomorphism and/or incorporation of impurity atoms (C, H) in the interstitial sites of Pd. While both contraction and expansion of the lattice have been reported experimentally, a common tendency from a theoretical perspective is converging to a shrinkage of the lattice parameter with downsizing, irrespective of the nature of metal nanoparticles.[4,46–52] Indeed, our TB calculations clearly demonstrate a fcc lattice contraction with reducing the Pd particle size, irrespective of cuboctahedra, icosahedra and truncated octahedra morphology, as detailed for different cluster sizes in Fig. SI-6† and related comments.

However, the present EXAFS refinements of bulk and nanosized clean Pd particles (free of surface oxidation and other interstitial impurities) have proven little change with size reduction: the nearest neighbour distance is 2.748 Å for bulk, 6.0 and 2.0 nm Pd while 2.745 Å was obtained for 1.4 nm Pd nanoparticles. This very slight contraction with size reduction is within the error bar of our refinements. Thus, the lattice of the Pd nanoparticles seems to be relaxed without any surface strain. The reason for this discrepancy with the TB modelling is still unknown and further investigations are needed to explain this behaviour, which is beyond our present aim. However, our main objective from atomic scale simulations is to study the effect of H trapping within Pd nanoparticles.

Size-dependence of trapped H in nanoparticles

The H trapping in the volume of nanosized Pd was proven by *in situ* EXAFS experiments and corroborated by the PCI findings. Moreover, a size-dependence of H trapping in Pd nanoparticles is uncovered: the smaller the size, the larger the content of trapped H, as also depicted in Fig. 4. Trapping of H in small Pd nanoparticles has been already reported for discrete sizes such as, 6.1 nm,[30] 3.6 nm (ref. 29) and 2.5 nm.[28] However, size-dependence of H tapping in Pd nanoparticles has never been reported previously, to the best of our knowledge.

The total amounts of absorbed H in Pd nanoparticles at 1 bar H_2 pressure and 25 °C are 0.65, 0.45 and 0.45 H/M for 6.0, 2.0 and 1.4 nm nanoparticles, respectively (from the PCI curves). The amount of trapped H can be calculated by dividing the expansion of the cell volume due to H trapping (from EXAFS results) per metal atom to the volume of the interstitial H atom in Pd. The latter one was determined from the variation of the lattice cell volume from bulk Pd metal to the hydride phase under 1 bar at 25 °C and the total amount of absorbed H in bulk Pd, as taken from the PCI curve. This value was found to be around 2.7(1) $Å^3$ per H atom, close to 2.9 $Å^3$ proposed by Peisl[53] for various hcp, bcc, and fcc metals and alloys. Using this approach, the quantities of trapped H in Pd nanoparticles are approximately 0.06, 0.12 and 0.12 H/M for 6.0, 2.0 and 1.4 nm Pd nanoparticles, respectively. These values represent around 9, 26 and 26% of the total H sorption capacity for nanoparticles with average sizes 6.0, 2.0 and 1.4 nm, respectively.

Consequently, the H trapping in Pd nanoparticles is increasingly important with decreasing the particle size. The amount of trapped H can be as high as 26% of the initial capacity for the smaller Pd nanoparticles (with 2.0 and 1.4 nm average sizes).

Location of trapped H in nanoparticles

From the point of view of desorption, we can distinguish several types of sites available for H: those with fast kinetics of desorption and the trapping sites with stronger binding energy. The desorption of H from the former is faster in nanoparticles than in Pd bulk due to short diffusion lengths and large surface area for H recombination. EXAFS results indicate that the

trapped H are located in the volume of nanoparticles without providing a clear localization of H within the core or the subsurface of nanoparticles.

To get insight at the atomic scale and investigate the stability of H inside the Pd nanoparticles, we performed DFT calculations. More precisely, the formation energy (E_f) of H inserted in octahedral or tetrahedral interstitial sites along the radius of the nanoparticle was calculated according to the following equation: $E_f = E_{Pd+1H} - E_{Pd} - 1/2E_{H_2}$, where E_{Pd+1H} is the total energy of the Pd system (fcc bulk or nanoparticle) containing one hydrogen atom, E_{Pd} is the total energy of the pure Pd system and E_{H_2} is the total energy of the H_2 molecule. The more negative E_f is, the more strongly the H atom is bound to neighboring Pd atoms. It is worth noting that the study of the complete desorption kinetics of H_2 is not our purpose but, above all, to identify the most stable thermodynamic position at the end of the desorption process. Moreover, at this stage of desorption a solid solution is formed within the NP. Thus, the calculation for only one H atom inserted in Pd nanostructure is relevant since H atoms do not interact directly with each other contrary to the case of hydride.

As a first step, we determined the most favorable interstitial site occupied by a hydrogen atom in a "bulk" fcc Pd containing 108 atoms. As seen in previous works,[54,55] among the two possible interstitial sites, the octahedral one is the most stable in the bulk, even if the energy difference between both interstitial sites is weak (around 0.1 eV). This stable configuration is not surprising since the octahedral site is larger than the tetrahedral one. Indeed, the presence of H in the tetrahedral site induces a local distortion (around 3% according to our calculations) required to relax the constraints, which is not the case for the octahedral position.

We now focus on nanoparticles containing 147 and 309 atoms in the cuboctahedron form. More precisely, the formation energy of H atoms located in interstitial sites along the radius of the nanoparticles, *i.e.* from the center to the outer surface, was calculated. The results are presented in Fig. 6, where only the case of a nanoparticle containing 309 atoms is depicted, since the same conclusions can be drawn for the 147 atoms nanoparticle.

First of all, for each location within the nanoparticle, the octahedral position is the most stable, in agreement with the bulk case. More interestingly, it is clearly observed that the further away from the core (surface and subsurface sites), the more stable the H atom (Fig. 6d). This is particularly true for H atoms occupying subsurface sites, which are the most stable configurations (red part in Fig. 6c and d). The energy gain of an atom located at the subsurface in comparison with a bulk position is significant in the order of 1 eV. Indeed, in the presence of a surface the relaxation process is easier and the elastic energy cost is lower. Analysis of the local distortions around the incorporated H atom clearly shows this effect (Fig. 6b). On the one

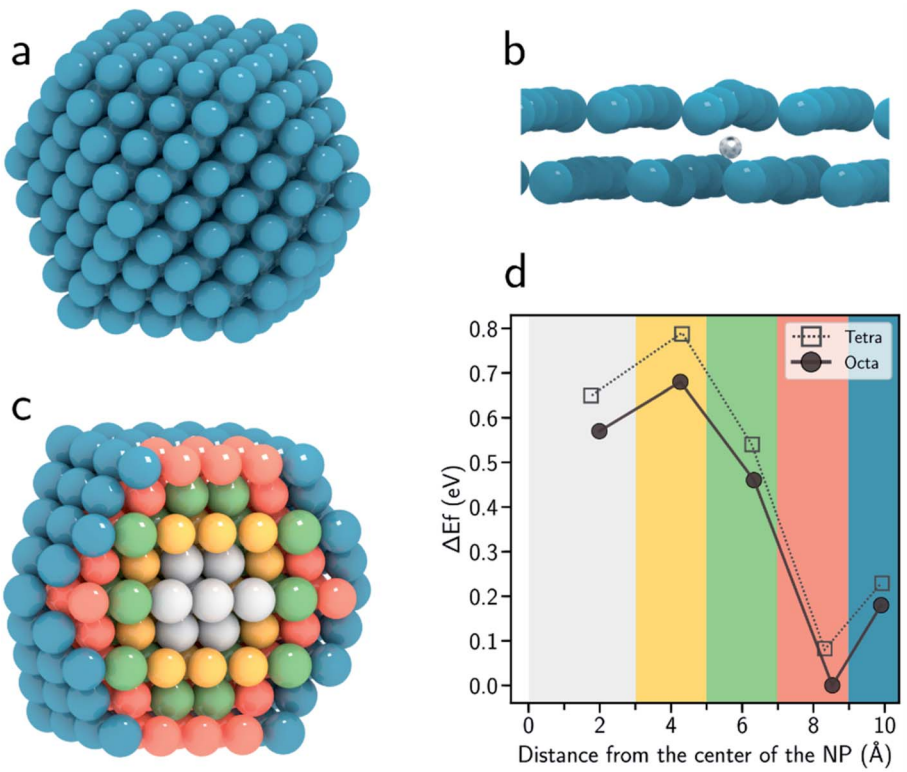

Fig. 6 (a) Cuboctahedron NP of Pd containing 309 atoms. (b) Presence of the hydrogen atom (white) in the subsurface position of the NP inducing a local distortion of the first layers. (c) Slide view showing the different planes within the NP. (d) Formation energy of a hydrogen atom occupying different sites (octahedral and tetrahedral) along the radius of the NP. The different coloured areas correspond to the regions indicated in (c): blue and red correspond to the surface and subsurface, respectively. The most stable configuration is set to zero.

hand, the H atom located at the core is strongly constrained and cannot distort the structure leading to low distortion (1%). In contrast, the H atom in the subsurface octahedral position can maximize the formation of Pd–H bonds, which are favorable, while at the same time it is able to strongly distort the structure to relax the stresses (around 7%). Such a configuration is more stable than in the surface position since by occupying an octahedral site, the H atom forms stronger bonds. As a result, the formation of Pd–H bonds and the elastic effect required to relax the structures favor the segregation of strongly energetic interstitial sites toward subsurface positions. It is to be noted that the subsurface position has often been put forward to explain the catalytic activity of transition or noble metals.[56,57] Consequently, our DFT calculations suggest that hydrogen atoms are trapped at subsurface sites that are very stable and more favorable than bulk sites. It can be noted that no significant difference was observed for the two sizes of nanoparticles considered in the present work (147 and 309 atoms), since they have fairly similar diameters (1.7 and 2.1 nm, respectively). In both cases, the H atoms at subsurface positions are strongly bound to the Pd atoms and therefore less prone to leave the particle at room temperature, as observed experimentally. A higher temperature, around 150 °C, is needed for complete H desorption from these trapping sites.

Conclusion

This report demonstrates the H trapping in the subsurface interstitial sites of Pd nanoparticles with 6.0, 2.0 and 1.4 nm average sizes by a combined experimental and theoretical approach. Interestingly, a double size dependent effect of H trapping inside Pd nanoparticles is highlighted experimentally: the smaller the Pd particle size, the larger the fraction of trapped H and the higher the binding energy experienced by these H atoms. Moreover, the trapped H can be desorbed by heating to around 150–170 °C under vacuum or inert gas flow. However, our experimental proofs could only confirm the trapping of H inside the volume of nanoparticles without a clear localization of these trapping interstitial sites. Our joint DFT and TB simulations suggest that the strong H trapping sites are located at the subsurface of nanoparticles, just beneath the surface.

This finding is crucial in the field of heterogeneous catalysis for which Pd is a widespread catalyst in many hydrogenation reactions. The quantity of trapped H is significant for Pd nanoparticles with sizes ≤2.0 nm and can reach one fourth of the maximum absorbed H. Thus, trapped H at the subsurface may play an important role in hydrogenation reactions through a subsurface hydrogen-induced electronic effect leading to the stabilization of metal–H bonds at the surface. Recently, the latter effect was shown to be beneficial for the hydrogenation of butadiene on RhH_X nanoparticles.[58] Finally, this finding may open the way for clarifying the controversial role of "subsurface or bulk" hydrogen in Pd-based nano-catalysts for various hydrogenation reactions.

Conflicts of interest

There are no conflicts to declare.

Acknowledgements

The authors acknowledge the French National Research Agency (ANR) for financial support (contract Ultracat ANR-17-CE06-0008-02). Yassine Oumellal is thanked for help with PCI measurements. Imerys Carbon & Graphite acknowledged for providing the HSAG-500 carbon. Stéphanie Belin is acknowledged for help during the XAS experiments on ROCK beam line at Soleil. This work was supported by a public grant overseen by the French National Research Agency (ANR) as part of the "Investissements d'Avenir" program (reference: ANR10-EQPX45).

References

1 Y. Zhao, Y. Wu, J. Liu and F. Wang, *ACS Appl. Mater. Interfaces*, 2017, **9**, 35740–35748.
2 E. Roduner, *Chem. Soc. Rev.*, 2006, **35**, 583–592.
3 R. Lamber, S. Wetjen and N. Jaeger, *Phys. Rev. B: Condens. Matter Mater. Phys.*, 1995, **51**, 10968.
4 C. Barreteau, M. C. Desjonquères and D. Spanjaard, *Eur. Phys. J. D*, 2000, **11**, 395–402.
5 C.-M. Lin, T.-L. Hung, Y.-H. Huang, K.-T. Wu, M.-T. Tang, C.-H. Lee, C. T. Chen and Y. Y. Chen, *Phys. Rev. B: Condens. Matter Mater. Phys.*, 2007, **75**, 125426.
6 W. A. Oates, *J. Less-Common Met.*, 1982, **88**, 411–424.
7 A. Pundt, C. Sachs, M. Winter, M. T. Reetz, D. Fritsch and R. Kirchheim, *J. Alloys Compd.*, 1999, **293**, 480–483.
8 A. Pundt and R. Kirchheim, *Annu. Rev. Mater. Res.*, 2006, **36**, 555–608.
9 C. Sachs, A. Pundt, R. Kirchheim, M. Winter, M. T. Reetz and D. Fritsch, *Phys. Rev. B: Condens. Matter Mater. Phys.*, 2001, **64**, 075408.
10 M. Yamauchi, R. Ikeda, H. Kitagawa and M. Takata, *J. Phys. Chem. C*, 2008, **112**, 3294–3299.
11 C. Zlotea and M. Latroche, *Colloids Surf., A*, 2013, **439**, 117–130.
12 C. Zlotea, Y. Oumellal, K. Provost and C. Matei Ghimbeu, *Front. Energy Res.*, 2016, **4**, 24.
13 A. Malouche, C. Zlotea and P. Á. Szilágyi, *ChemPhysChem*, 2019, **20**, 1282–1295.
14 A. Malouche, G. Blanita, D. Lupu, J. Bourgon, J. Nelayah and C. Zlotea, *J. Mater. Chem. A*, 2017, **5**, 23043–23052.
15 A. Züttel, Ch. Nützenadel, G. Schmid, D. Chartouni and L. Schlapbach, *J. Alloys Compd.*, 1999, **293–295**, 472–475.
16 C. Nützenadel, A. Züttel, D. Chartouni, G. Schmid and L. Schlapbach, *Eur. Phys. J. D*, 2000, **8**, 245–250.
17 J. A. Eastman, L. J. Thompson and B. J. Kestel, *Phys. Rev. B: Condens. Matter Mater. Phys.*, 1993, **48**, 84–92.
18 J. Weissmuller and C. Lemier, *Philos. Mag. Lett.*, 2000, **80**, 411–418.
19 S. Wagner and A. Pundt, *Int. J. Hydrogen Energy*, 2016, **41**, 2727–2738.
20 T. P. Senftle, M. J. Janik and A. C. T. van Duin, *J. Phys. Chem. C*, 2014, **118**, 4967–4981.
21 M. Ruda, E. A. Crespo and S. R. de Debiaggi, *J. Alloys Compd.*, 2010, **495**, 471–475.

22 E. A. Crespo, M. Ruda, S. Ramos de Debiaggi, E. M. Bringa, F. U. Braschi and G. Bertolino, *Int. J. Hydrogen Energy*, 2012, **37**, 14831–14837.
23 C. Nützenadel, A. Züttel, D. Chartouni, G. Schmid and L. Schlapbach, *Eur. Phys. J. D*, 2000, **8**, 245–250.
24 C. Sachs, A. Pundt, R. Kirchheim, M. Winter, M. T. Reetz and D. Fritsch, *Phys. Rev. B: Condens. Matter Mater. Phys.*, 2001, **64**, 075408.
25 A. Pundt, M. Suleiman, C. Bahtz, M. T. Reetz, R. Kirchheim and N. M. Jisrawi, *Mater. Sci. Eng., B*, 2004, **108**, 19–23.
26 B. J. Heuser, D. R. Trinkle, T.-N. Yang and L. He, *J. Alloys Compd.*, 2013, **577**, 189–191.
27 Y.-W. You, X.-S. Kong, X.-B. Wu, Y.-C. Xu, Q. F. Fang, J. L. Chen, G.-N. Luo, C. S. Liu, B. C. Pan and Z. Wang, *AIP Adv.*, 2013, **3**, 012118.
28 D. Jose and B. R. Jagirdar, *Int. J. Hydrogen Energy*, 2010, **35**, 6804–6811.
29 H. Ren and T.-Y. Zhang, *Mater. Lett.*, 2014, **130**, 176–179.
30 H. Kobayashi, M. Yarnauchi, H. Kitagawa, Y. Kubota, K. Kato and M. Takata, *J. Am. Chem. Soc.*, 2008, **130**, 1828–1829.
31 S. Wagner, A. Pundt and Karlsruhe Institute of Technology (KIT), *AIMS Mater. Sci.*, 2020, **7**, 399–419.
32 S. Bastide, C. Zlotea, M. Laurent, M. Latroche and C. Cachet-Vivier, *J. Electroanal. Chem.*, 2013, **706**, 33–39.
33 C. La Fontaine, L. Barthe, A. Rochet and V. Briois, *Catal. Today*, 2013, **205**, 148–158.
34 A. Michalowicz, J. Moscovici, D. Muller-Bouvet and K. Provost, *J. Phys.: Conf. Ser.*, 2009, **190**, 012034.
35 A. Michalowicz, J. Moscovici, D. Muller-Bouvet and K. Provost, *J. Phys.: Conf. Ser.*, 2013, **430**, 012016.
36 C. Zlotea, Y. Oumellal, M. Msakni, J. Bourgon, S. Bastide, C. Cachet-Vivier and M. Latroche, *Nano Lett.*, 2015, **15**, 4752–4757.
37 C. Zlotea, C. Chevalier-Cesar, E. Leonel, E. Leroy, F. Cuevas, P. Dibandjo, C. Vix-Guterl, T. Martens and M. Latroche, *Faraday Discuss.*, 2011, **151**, 117–131.
38 H. Amara, J.-M. Roussel, C. Bichara, J.-P. Gaspard and F. Ducastelle, *Phys. Rev. B: Condens. Matter Mater. Phys.*, 2009, **79**, 014109.
39 F. Ducastelle, *J. Phys.*, 1970, **31**, 1055–1062.
40 D. J. Earl and M. W. Deem, *Phys. Chem. Chem. Phys.*, 2005, **7**, 3910–3916.
41 D. Frenkel and B. Smit, *Understanding Molecular Simulation*, Elsevier, 2002.
42 P. Giannozzi, S. Baroni, N. Bonini, M. Calandra, R. Car, C. Cavazzoni, D. Ceresoli, G. L. Chiarotti, M. Cococcioni, I. Dabo, A. D. Corso, S. de Gironcoli, S. Fabris, G. Fratesi, R. Gebauer, U. Gerstmann, C. Gougoussis, A. Kokalj, M. Lazzeri, L. Martin-Samos, N. Marzari, F. Mauri, R. Mazzarello, S. Paolini, A. Pasquarello, L. Paulatto, C. Sbraccia, S. Scandolo, G. Sclauzero, A. P. Seitsonen, A. Smogunov, P. Umari and R. M. Wentzcovitch, *J. Phys.: Condens. Matter*, 2009, **21**, 395502.
43 P. E. Blöchl, *Phys. Rev. B: Condens. Matter Mater. Phys.*, 1994, **50**, 17953–17979.
44 J. P. Perdew, K. Burke and M. Ernzerhof, *Phys. Rev. Lett.*, 1996, **77**, 3865–3868.
45 T. Ohba, H. Kubo, Y. Ohshima, Y. Makita, N. Nakamura, H. Uehara, S. Takakusagi and K. Asakura, *Chem. Lett.*, 2015, **44**, 803–805.
46 Q. Jiang, L. H. Liang and D. S. Zhao, *J. Phys. Chem. B*, 2001, **105**, 6275.
47 G. Ouyang, X. L. Li, X. Tan and G. W. Yang, *Appl. Phys. Lett.*, 2006, **89**, 031904.
48 G. Ouyang, W. G. Zhu, C. Q. Sun, Z. M. Zhu and S. Z. Liao, *Phys. Chem. Chem. Phys.*, 2010, **12**, 1543–1549.
49 X. J. Liu, Z. F. Zhou, L. W. Yang, J. W. Li, G. F. Xie, S. Y. Fu and C. Q. Sun, *J. Appl. Phys.*, 2011, **109**, 074319.
50 Z. Huang, P. Thomson and S. Di, *J. Phys. Chem. Solids*, 2007, **68**, 530–535.
51 W. H. Qi and M. P. Wang, *J. Nanopart. Res.*, 2005, **7**, 51–57.
52 W. Qi, B. Huang and M. Wang, *Nanoscale Res. Lett.*, 2009, **4**, 269.
53 H. Peisl, in *Hydrogen in Metals I*, ed. G. Alefeld and J. Völkl, Springer Berlin Heidelberg, Berlin, Heidelberg, 1978, vol. 28, pp. 53–74.
54 Y. Fukai, *The Metal-Hydrogen System*, Springer-Verlag., Berlin/Heidelberg, 2005, vol. 21.
55 B. Lin, X. Wu, L. Xie, Y. Kang, H. Du, F. Kang, J. Li and L. Gan, *Angew. Chem., Int. Ed.*, 2020, **59**, 20348–20352.
56 D. Teschner, J. Borsodi, A. Wootsch, Z. Révay, M. Hävecker, A. Knop-Gericke, S. D. Jackson and R. Schlögl, *Science*, 2008, **320**, 86–89.
57 H. A. Aleksandrov, S. M. Kozlov, S. Schauermann, G. N. Vayssilov and K. M. Neyman, *Angew. Chem., Int. Ed.*, 2014, **53**, 13371–13375.
58 F. Morfin, L. Blondeau, K. Provost, A. Malouche, L. Piccolo and C. Zlotea, *Catal. Sci. Technol.*, 2018, **8**, 2707–2715.